CT-scan in-situ investigation of waterflood front instabilities during immiscible displacements: effect of viscosity contrast and flow rate

Matthieu Mascle[1,*], *Elisabeth* Rosenberg[1], *Berit* Roboele[2], *Espen* Kowalewski[2], and *Souhail* Youssef[1]

[1]IFP Energies Nouvelles, Geofluids & Rock Department, 92852 Rueil-Malmaison Cedex, France
[2]Equinor ASA, 7005 Trondheim, Norway

Abstract. In this work, unstable displacements were conducted using special equipment designed to run in-situ CT-scanner experiments. All the displacements were conducted on a strongly water-wet Bentheimer sandstone full-size plug, of 10cm in diameter and 40cm in length. It was found that the oil recovery at brine breakthrough (%PV) shows a good correlation with the viscous fingering number as defined by Doorwar. Early water breakthrough appears to be boosted by high injection flow rate and less favorable fluids mobility ratio. The local saturation monitoring provides new insight to characterize the finger shapes and analyze the production mechanisms, for the different flowing conditions. In water-wet conditions, the capillary forces contribute to stabilize the front against viscous instabilities. If the viscous forces become too dominant, the capillary forces are overcome and fingering may occur for displacement with unfavorable fluids ratio. A diagram has been constructed to separately quantify the contribution of the viscous fingering and the capillary fingering. Results have shown that capillary fingering was the main mechanism responsible for the water early breakthrough.

1. Introduction

Unstable displacements can occur when a fluid is displaced by any fluid of different nature. The driving force of these instabilities can either be a viscosity contrast, a density contrast or capillary forces when the two considered fluids are immiscible. As these complex flows lead to poor fluids mixing or sweeping efficiency and early fluid breakthrough (BT), they have been discussed in an extensive number of publications of various engineering fields [1–4].

When the displacing and displaced fluids are immiscible, the front instabilities take the form of fingering. Their shape and magnitude are governed by various parameters, including the fluids and rock properties and structure, the injection conditions or the system dimensions and heterogeneities. Previous authors have suggested dimensionless scaling parameters aiming to account for all these contributions. Among the first, Peters and Flocks [5] have constructed a dimensionless number (I_{sc}) using Chuoke's stability theory [6] to predict the onset of front instabilities. Later, Lenormand et al. [7] proposed a phases-diagram using two dimensionless numbers to dissociate the capillary and the viscous contributions (C and M, respectively). Their diagram provided a better characterization of the different flow instabilities forms, with 3 identified regimes: (1) a piston-like displacement in the stable flow domain, (2) high magnitude tree-like fingerings in the viscous dominated flow domain and (3) low magnitude loop-like fingering in the capillary dominated flow domain. More recently, Doorwar [8] combined Lenormand two dimensionless numbers and added a tertiary contribution to account for the core dimensions and petrophysical properties. This contribution was already expressed in Peters and Flocks instability number. The resulting dimensionless number N_I has demonstrated good results to predict total fluids recovery at BT (BTR) for water-wet displacement, but provide no forecast for fluids fingering shape.

Fingering occurs at different scales ranging from the phases by-pass at pore level to the phases partitioning at reservoir level. The magnitude of their dimensions variation causes its modelling to be a perilous task using Darcy's scale models [9]. One solution is to upscale flow dynamics properties from laboratory experiments, to account for the complexity of these flows at higher scale resolution. In recent works, various authors [10–12] have used and adapted Fayers' phenomenological approach of viscous fingering [13] to upscale relative-permeabilities. These models, referred as lumped-finger, rely on the merging of all fingering in a unique finger, described by various physical parameters. This approach allows to obtain a satisfying match of the global experimental data (mean saturation or total pressure drop). Yet, the local saturations and the equivalent finger shape is rarely studied. The phenomenological modelling demonstrates the necessity to have a 2D or 3D flow visualization to characterize front inabilities forms. Glass micro-models had provided a useful tool for visual inspection but they are limited in dimensions and connectivity [12, 14]. Slab

* Corresponding author: matthieu.mascle@ifpen.fr

experiments conducted on Bentheimer samples have allowed to look further in the 2D fingerings characterization [9, 15]. However, the core width is restricted with these experiments, leading to high dimensions ratio. It has been demonstrated that this dimensions ratio strongly affect the fingers growth [12]. Molding techniques using epoxy resin have been used on real cores in the past [16] to show the complexity of the fluids front. But this method obviously does not allow for any dynamic monitoring.

In this work, unstable displacements were conducted using special equipment designed to run experiments combined with a CT-scanner. All the displacements were conducted on a strongly water-wet Bentheimer sandstone full-size plug, of 10cm in diameter and 40cm in length. A set of waterflood displacements have been conducted in a coreflood cell with different oil viscosity (from 5 to 330 cP) and injection flowrate (from 85 cc/h to 420 cc/h) to assess their effect on the front stability. The purpose of this work is to characterize the finger shapes and analyze the production mechanisms, for the different flowing conditions.

2. Materials and methods

2.1 Coreflood set-up

An overview of the experimental set-up is given Fig. 1. Experiments were conducted using a special equipment designed to run in-situ experiments under a CT scanner. The equipment is composed of an X-ray transparent core holder and a mobile rig able to inject different fluids at up to 100bar. The core holder is designed to handle cylindrical samples of 10cm in diameter and up to 60cm in length. The core holder body is made of a 5mm thickness aluminum alloy which allows good X-ray transmission at an energy of 140kVP.

A multi-pump system is used, allowing to inject different fluids without need of changing pump fluid and thus avoid fluid pollution. The low viscosity fluids are injected using Vindum VP-12K pumps. The high viscosity fluids are injected using 5L piston cylinders, connected to a Vindum pump to drive the pistons. The back pressure (BPR) is regulated to 20bars. The confining pressure is imposed to 50bars using an Isco syringe pump, fed with deionized water (MilliQ). Experiments are conducted at scanner room temperature, regulated by an air conditioner at 19.5°C.

Fig. 1. Overview of the IFPEN medical CT Scan GEHC Discovery 750HD and the experimental setup

The differential pressure is monitored using two 150 bar Keller absolute pressure transducers connected to the upstream and downstream static fluids lines. The fluids saturation is monitored using a medical CT scanner GEHC Discovery 750HD dual energy. It is operated at 140kVP with a beam current of 260mA to minimize signal/noise ratio. This equipment imposes the coreflood cell to be installed horizontally. The produced effluents are collected and gravity-separated in a vertical graduated burette to support the saturation computation.

2.2 Rock sample and fluids

A 4inch diameter, 40cm long water-wet Bentheimer core is used for the coreflood (Table 1). The core was analyzed with the dual energy mode of GEHC called GSI (Gemstone Spectral Imaging) to assess the saturation homogeneity (Fig. 2). It suggests the saturation is slightly increasing from the left to the right (from inlet to outlet). A small heterogeneity shaped as a 1cm radius sphere is visible near the center of the core. This centimeter-scale heterogeneity won't impact the flooding experiments. Still, it shows the Bentheimer rock-type can exhibit some heterogeneities. The mean porosity was estimated to 22.2%, giving a core pore volume (PV) of 722cc. The core permeability K was measured with the brine at a confining pressure of 50bar and a pore pressure of 20bar. The resulting permeability is estimated to 2530mD.

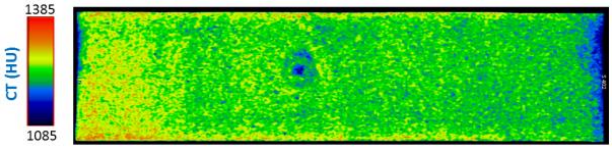

Fig. 2. CT Sagittal cross section rendering of the 10 cm diameter core. High CT values (hot shades) indicates lower porosities.

Table 1. Core dimensions and petrophysical properties

Dimensions (D, L)	10cm, 40cm
Mean porosity Φ	22.2%
Absolute permeability K	2530mD
Dispersion D	2.7 10^{-9}m²/s

Experiments have been conducted using a 70 g/l TDS brine and mineral oils with different viscosities (Isopar L, Primol and Drakeol). The brine water is a mixture of NaCl (30g/L) doped with NaI (40g/L) to increase the CT contrast. The viscosity of the different mineral oils was estimated at 19.5°C. The resulting viscosities are respectively for the Drakeol, the Primol and the Isopar L: 321cP, 168cP and 4.7cP. The estimated viscosity for brine using tabulated data is 1.18cP. Deionized water (MilliQ) and isopropyl alcohol (IPA) were used for cleaning and miscible fluids exchange. Viscosities and densities of the different fluids used in this study are summarized Table 2. The interfacial tension (IFT) of the mineral oil in contact

with the brine has been measured using the Wilhelmy plate method.

Table 2. Fluid properties at 19.5°C, and interfacial tension (IFT in contact with the brine water).

Fluid	Viscosity (cP)	Density (g/cc)	IFT (mN/m)
Brine	1.18	1.05	-
Drakeol	321	0.86	51
Primol	168	0.86	30
Isopar L	4.7	0.76	45

The core homogeneity is assessed using a tracer test. The brine water was injected at 7.0cc/min in the core saturated with the MilliQ water. The tracer concentration is monitored using the CT-scanner. Concentration profiles are given Fig. 3, with the local value displayed on the sagittal core section (see section 2.4). They show a homogenous displacement with limited phases dispersion during the sweeping. This core dispersion is fitted to $D = 2.7{\cdot}10^{-9} m^2/s$ using an analytical solution [17] (Fig. 4).

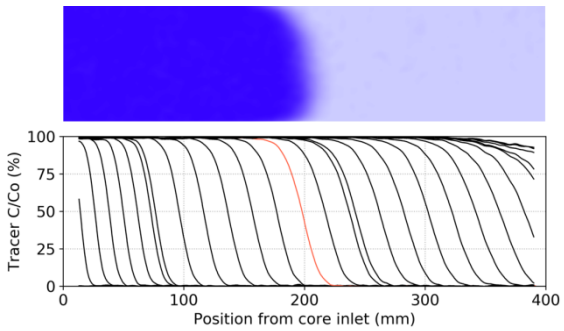

Fig. 3. Tracer concentration profiles during a tracer injection. The red profile and the sagittal section are taken after 0.5PVinjected.

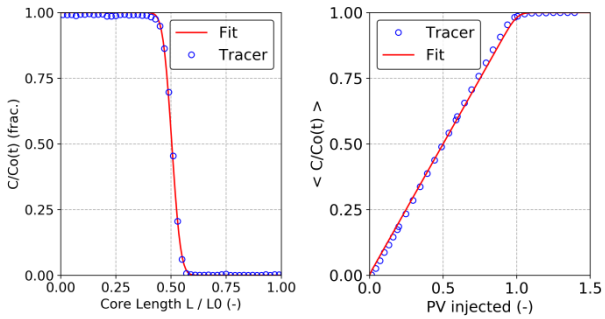

Fig. 4. Core dispersion fitted using an analytical solution [17]. The dispersion is fitted using the concentration profile after 0.5PV injected (left plot) and total tracer concentration (right plot). Dispersion is fitted to $2.7{\cdot}10^{-9}$ m²/s.

2.3 Experimental procedure and design

Five waterflood displacements have been conducted on the same Bentheimer core using varying injection flow-rates and oil viscosities. All the fluids were injected from the same inlet face. Corefloods with the Primol (CF2 and CF3) were conducted first, followed by the coreflood with the Isopar L (CF1). Corefloods with the Drakeol (CF4 and CF5) were conducted at last due its higher viscosity. All experiments start at *Swi*, reached by injecting the oil at 180cc/h, until pressure and saturation stability are obtained. From *Swi*, the brine is injected for a minimum of 5 pore-volumes. Both the differential pressure and the fluids saturation are monitored during this displacement. After the water flooding, the oil used in the next coreflood is directly injected to reach *Swi* and replace the oil from the previous experiment. For CF1, *Swi* is set by flooding with the Primol first, followed by Isopar L injection to replace the Primol. This intermediate step is conducted with the Isopar L oil to have comparable *Swi* for all experiments, considering its low viscosity possibly leading to unfavorable displacement.

The core entry face is swept with brine before proceeding with the injection in the core, using a dedicated outlet port in the inlet face. Homogenous sweeping is ensured by an injection diffuser carved with a double spiral. During the sweeping phase, the flow rate is set to 50cc/h for at least 2h. This step is monitored using the CT-scan for quality-checking. The experimental design of the presented experiments is given in Table 3. Peters & Flocks instability number I_{sc} [5] is computed for each displacement, using equation 1, where μ_o and μ_w respectively expressed the oil and brine water viscosity, v is the brine superficial velocity, K is the core absolute permeability, σ_{ow} is the fluids interfacial tension and C^* is the dimensionless wettability number, taken to 306 for water-wet core [5]. In their theory, they predicted unstable displacements for $I_{sc} > 13.56$. Following this, all waterflood displacement excepted CF1 are expected to show instabilities.

$$I_{sc} = \left(\frac{\mu_o}{\mu_w} - 1\right)\frac{v\mu_w D^2}{C^*\sigma_{ow}K} \qquad (1)$$

Table 3. Experimental corefloods design, with the I_{sc} instability number computed (see equation 1).

Coreflood	Oil (viscosity)	Injection flow rate (cc/min)	I_{sc}
CF1	Isopar L (4.7cP)	7.0	4
CF2	Primol (168cP)	1.4	50
CF3	Primol (168cP)	7.0	250
CF4	Drakeol (321cP)	1.4	56
CF5	Drakeol (321cP)	7.0	280

2.4 Saturation monitoring

The full core is scanned in 30sec which allowed to acquire 3D images with a time interval of 3min until breakthrough and 20min after. Voxel resolution was 0.33x0.33x1.25mm. The local saturation is computed from

the CT-scans using a linear scaling of the fluids X-ray contrast between its two extreme saturation states (referred to as CT-references), given by equation 2. Illustrations of 2D of the local saturation is given Fig. 5, in sagittal and transverse slicing. A mean-filter is used with a kernel of 3^3 voxels to reduce the noise.

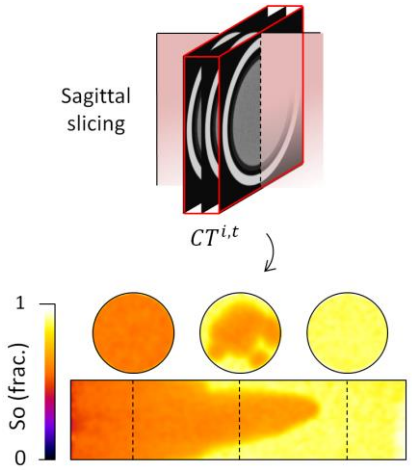

Fig. 5. Illustration of sagittal and transverse slicing processing from raw data.

CT-references are acquired for all the fluids under consideration, with the core saturated with the corresponding fluid (Fig. 6). The average CT-contrast between the brine and the oils is 157HU (Hounsfield Unit) for the Isopar L and 135HU for the Drakeol and Primol.

$$S_o^{i,t} = (CT^{i,t} - CT_{oil}^{i}) / (CT_{brine}^{i} - CT_{oil}^{i}) \qquad (2)$$

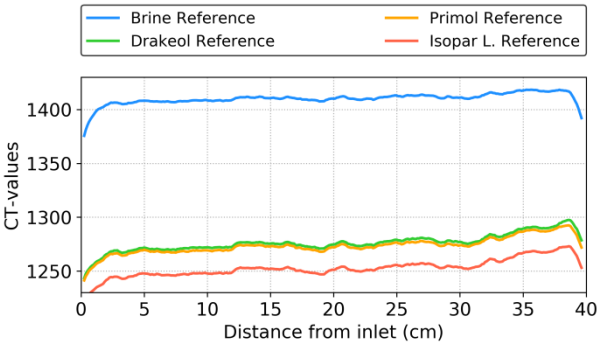

Fig. 6. CT-references of the brine water and the mineral oils

Repeatability and stability measurements conducted on the CT-scanner have given a standard error δCT equal to 1HU. An estimation of the standard error δSo can be done according to equations 2 and 3. The standard error is lower than 1% for all experiments. Confidence intervals (IC95) are plotted Fig. 7 for the 3 mineral oils. IC95 (and therefore the standard error) is lower for the Isopar L oil due to its higher CT-contrast with the brine.

$$\delta S_o{}^2 = \delta CT^2 \left(\frac{\delta S_o}{\delta CT^i}^2 + \frac{\delta S_o}{\delta CT_{brine}}^2 + \frac{\delta S_o}{\delta CT_{oil}}^2 \right) \qquad (3)$$

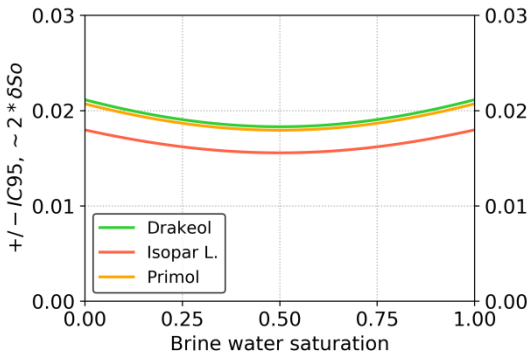

Fig. 7. Saturation confidence intervals (IC95) computed for the different minerals oil. IC95 is computed as twice the standard error δSo. δSo is computed using equations 2 and 3.

The scanner resolution prevents us to 3D render the water fingering occurring at low scale (< 1.25mm). Consequently two types of fingerings are considered here: 1, the macroscopic fingering that has a higher magnitude than the scanner resolution and 2, the local fingering that has a lower magnitude than the scanner resolution. The macroscopic fingering is easily characterized using the CT-images. The local fingering (interpreted capillary fingering) is characterized using the local oil saturation in the swept areas.

3. Results and discussion

3.1 Water breakthrough (BT)

The dynamic core oil saturations measured using the CT-scanner during waterflood are compared in Fig. 8 for the 5 corefloods. The differential pressures recorded during the flooding are given in Fig. 9. The *Swi* reached after oil drainage are comparable for all corefloods, ranging from 11.3 to 12%. The water flooding with the lowest oil viscosity (CF1) shows a remarkable piston-like displacement, with no oil produced after breakthrough (BT). All other corefloods (CF2 to CF5) show early BT compared to CF1, with a different arrival time for each. These observations are consistent with Peter & Flocks instability number I_{sc}, that predicted stable displacement for CF1, and unstable displacements for the others corefloods (Table 3).

Results obtained in this study show that the fingering increases by increasing water injection flow rate or decreasing fluids viscosity ratio (defined as μ_w/μ_o). This is in agreement with most of the results found in the literature for the water-wet case [12]. Still, it is not clear why the fingering is boosted with high injection flow rate at constant mobility ratio, as the opposite trend was observed for the oil-wet case [11].

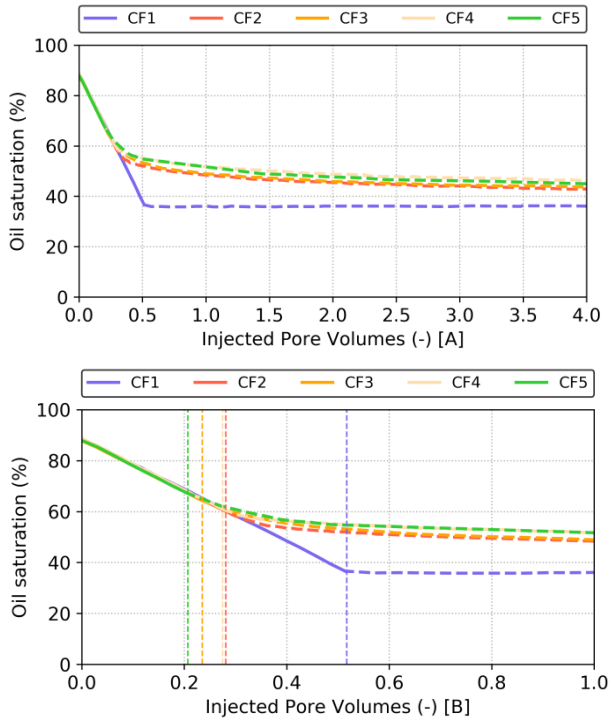

Fig. 8. Core oil saturation comparison during the coreflood [A], zoomed on the 1 first injected pore volume [B]. Plain lines are before breakthrough, dashed lines are after breakthrough (separation is indicated by the vertical dotted lines).

The differential pressure (dP) recorded during CF1 coreflood shows a specific trend with an increase of the pressure losses from *Swi* to *Sorw*, despite the oil being replaced by a less viscous fluid (Fig. 9). A similar behavior was observed by Doorwar [12] for the most favorable displacement ($\mu_w/\mu_o = 1$). This behavior can be explained by the water-wet nature of the core and the piston-like displacement. For the other cores, the oil viscosities being substantially higher than the brine water's, the dP decreases as the oil is swept.

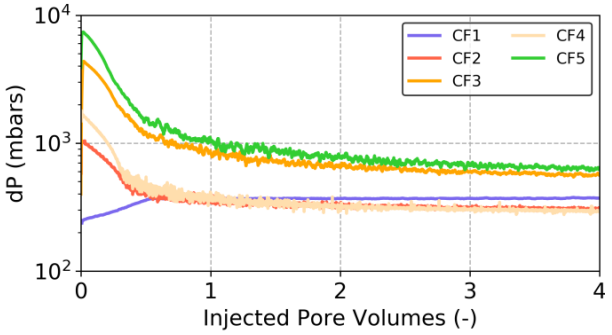

Fig. 9. Differential pressure (dP) recorded during the corefloods.

The easiest and standard way to quantify the breakthrough time is to measure the quantity of water injected in the core until BT (PV@BT). This quantity is referred in this paper as the oil recovery at breakthrough (%PV). It is calculated using the oil saturation reached at breakthrough *So@BT* (see equation 4). These values are measured and summarized Table 4 for all corefloods. They are plotted in Fig. 10 as function of the instability number N_I defined by Doorwar in his thesis [8] (see equation 5).

$$Oil\ recovery\ @BT\ =\ 100 - Swi - So@BT \qquad (4)$$

$$N_I = \frac{v\mu_w}{\sigma_{ow}}\left(\frac{\mu_o}{\mu_w}\right)^2 \frac{D^2}{K} \qquad (5)$$

Results from Doorwar thesis of coreflood experiments conducted on a water-wet Boise sandstone (*Φ, D, L, K* = 29%, 5cm, 30cm, 6D, respectively*)* are included in the plot for comparison. Results obtained in this study demonstrate a comparable trend but do not align with Doorwar's data. A possible improvement of the Doorwar number, to scale all data, could be to integrate the fluids mobilities upstream and downstream of the front vicinity (referred as the shock mobility ratio), as suggested by previous authors [3, 18]. This shock mobility ratio may provide a better prediction of the front instability than the fluids viscosities solely.

Table 4. Saturations reached during the corefloods. The oil recovery at breakthrough is measured as: *Oil recovery @BT = 100 – Swi – So@BT*

Coreflood	Swi (%)	So@BT (%)	*Oil recovery @BT (%PV)*
CF1	11.7	38.05	50.25
CF2	11.7	60.4	27.9
CF3	12	66	22
CF4	11.9	61.2	26.9
CF5	11.3	69.45	19.25

Here, the monotonous increase of the breakthrough timing with respect to N_I has been fitted with a logarithmic regression to underline the global trend in the data. The number of data points presented here and considering its uncertainty associated is not sufficient to truly demonstrate the consistency of this regression. Logarithmic trends can be easily mistaken with power-law trend [19].

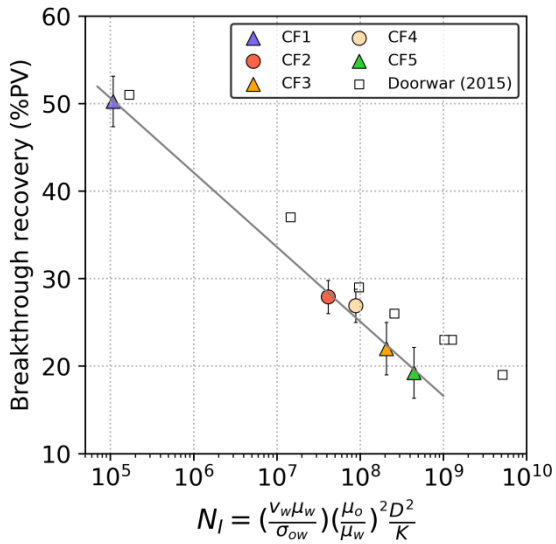

Fig. 10. Oil recovery at breakthrough (%PV) versus the Doorwar instability number N_I. The displayed bars errors account for the saturation confidence intervals and the temporal resolution of the

CT-monitoring. Circle and triangle markers respectively refer to corefloods conducted at 1.4 and 7.0 cc/min.

The saturation profiles, derived from the CT-scans, are given Fig. 11 for different time steps. They provide a beginning of answer to explain the early breakthrough for CF2 to CF5. The saturation profiles of these corefloods suggest a displacement far from being piston-like, especially when compared to CF1. The saturation profiles for CF1 provide additional insight to explain the increasing differential pressure observed during the displacement (Fig. 9). The piston-like displacement results in a spatially short transition of local saturations from *Swi* values, ahead the water-front, to *Sorw* values, behind it. In this configuration, mainly oil is flowing head of the front, and mainly brine-water is flowing behind the front. The pressure drop from inlet to outlet is consequently driven by two values: the oil relative permeability at *Swi* and the water relative permeability at *Sorw*, respectively referred as k_{rom} and k_{rwm}. An increasing differential pressure during a piston-like flooding, simply requires to have $k_{rwm} < k_{rom} * \mu_w/\mu_o$.

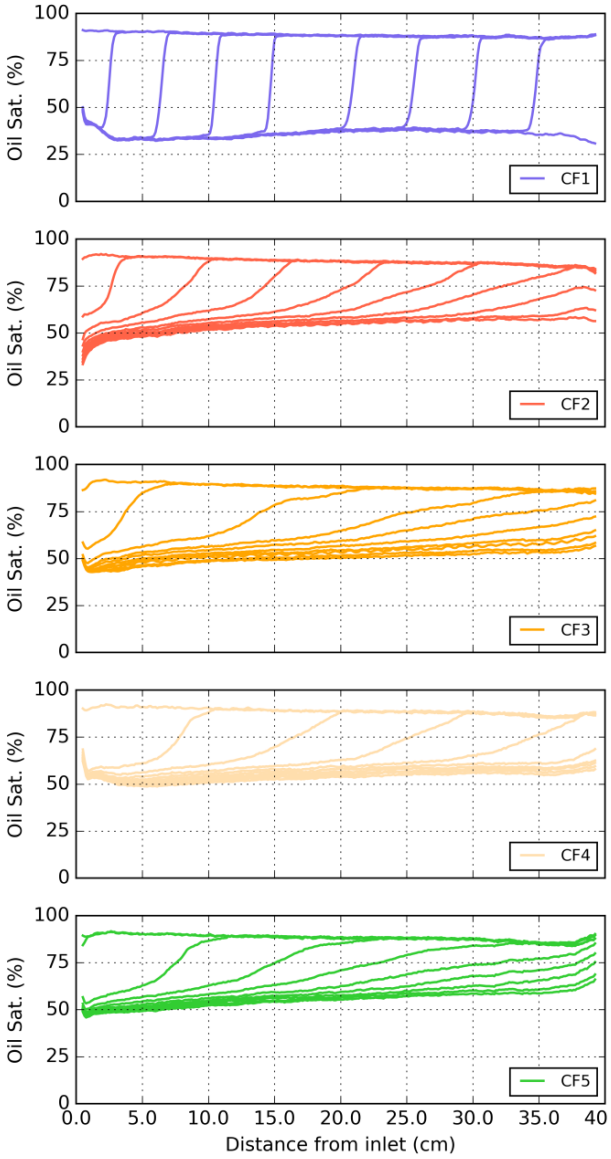

Fig. 11. Oil saturation profiles along the core axis for all corefloods.

The saturation profiles alone provide a poor characterization the finger's shapes. The next section uses the 3D CT-scans to better visualize the front instabilities.

3.2 Front instability shape

2D visualizations of the fingering are presented in Fig. 12 using sagittal and 3 transverse slicing. Positions of the transverse slicing are marked by the dotted black lines, at 8, 20 and 32cm from the core inlet. The sagittal slicing is illustrated in Fig. 5. Visualizations are given at breakthrough (on the right) and around half the breakthrough (on the left).

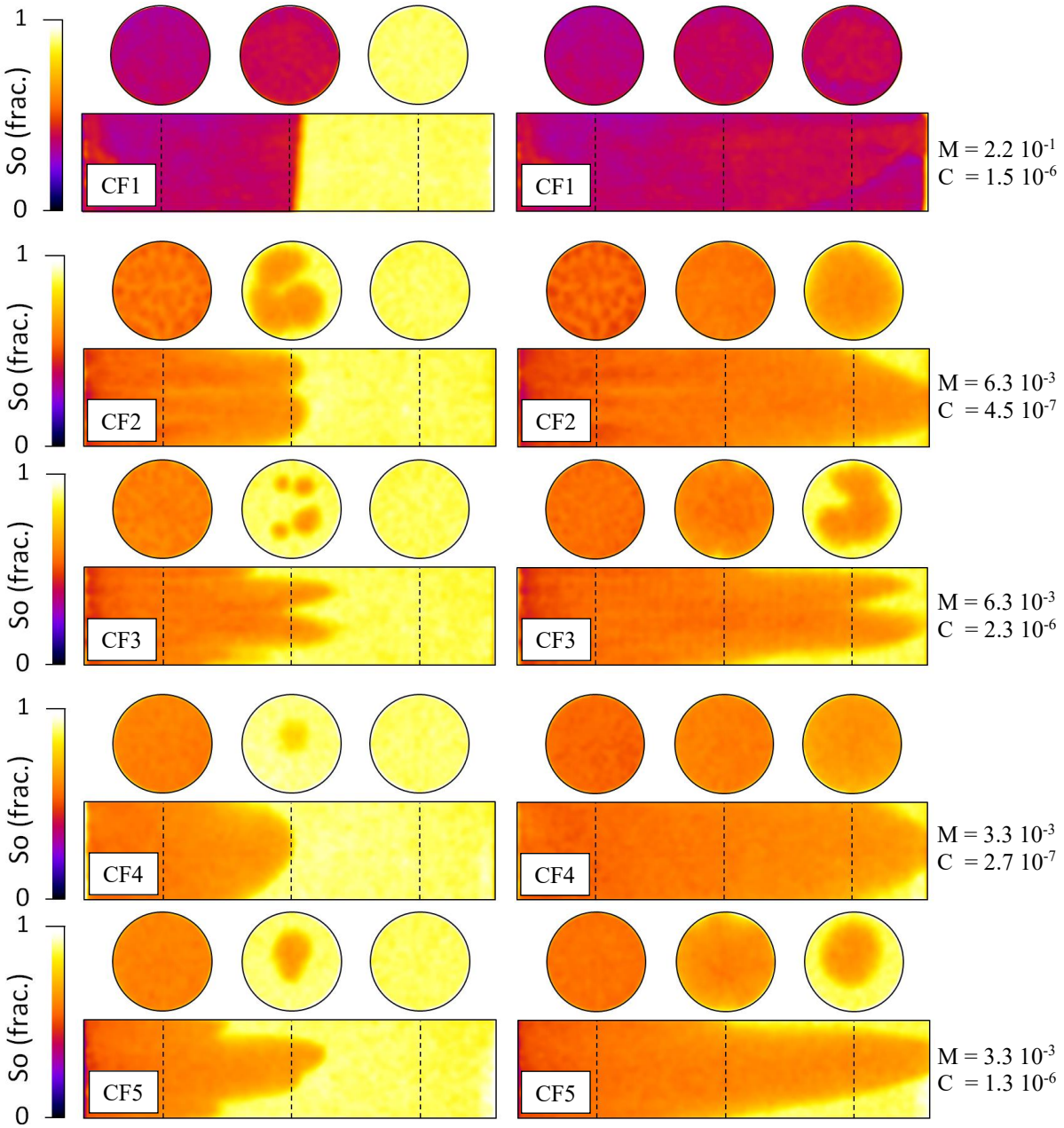

Fig. 12. 2D visualization if the front instability using sagittal and transverse slicing. The displacement is displayed at half the breakthrough on the left and at breakthrough on the right. Positions of the transverse slicing are marked by the dotted black line. The sagittal slicing is illustrated Fig. 5. M and C values are given on the right for each experiment.

The piston-like displacement is clearly visible for the coreflood CF1. The water front is completely stable, resulting in a homogenous sweeping of the core. This coreflood was expected to show the best oil recovery but not to have a perfect front stability, as the fluids mobility ratio is still unfavorable (μ_w/μ_o < 0.25 for CF1). This dynamic behavior may be explained by strong capillary forces, caused by the preferential core's wettability to water. Capillary forces generate a spontaneous invasion of the water in the core that overcomes the viscous instabilities and stabilizes the water front. It results in a front sharper than the monophasic fluids dispersion observable during a miscible displacement (see Fig. 3). Here, capillary forces have a dual contribution as they improve the sweeping efficiency at core-scale but are responsible for oil trapping at pore-scale (final *Sorw* is measured to 38%).

Results given Table 4 showed greater fingering as the flow rate is increased. This observation is consistent with the previous explanation: when the flow rate is increased, the capillary forces are overcome by the viscous forces. They can no longer stabilize the water front, resulting in more viscous fingerings. As capillary forces are related to the core's wettability, the trend suggested by our experiments between the breakthrough earliness and injection flow rate may only be valid for the water-case.

All others corefloods from this study (CF2 to CF5) show front instabilities taking the form of a main large finger or multiple fingers. CF2 and CF3, conducted with the Primol, have fingering slightly more complex than the fingering obtained with the Drakeol (CF4 and CF5). Experiments with the Primol exhibit up to 4 distinct fingers while it takes the form of a main, central finger with the Drakeol. It should be noted that the shape of the front is changing during the flooding leading to the progressive fingers merging. Despite the visible front instabilities for CF2 to CF5, the core is overall well swept at breakthrough. For all corefloods, the middle core cross-section shows a complete sweeping at breakthrough (Fig. 5). fingering is not as severe as it can be seen in slab experiments or in micro-models [7, 9, 15], where oil recovery at breakthrough (%PV) < *0.1* can be achieved. The comparison of the oil recoveries behind the water front (in the swept area) suggests that the early breakthrough is possibly mainly due to a lower oil recovery in the swept areas. Oil saturation behind the water front is measured around 38% for CF1 while it comes close to 60% for the others corefloods.

The experiments conducted here are represented on Fig. 13 in a manner following a Lenormand et al. phase-diagram [7]. This diagram represents the displacement regimes that may be expected according to two dimensionless numbers: the capillary and the viscous numbers (*C* and *M*, respectively). This diagram is probably too simplistic as it excludes the viscous and capillary fingering mechanisms to occur at the same time. It does provide, however, a global representation of the prevailing fingering mechanism which may occur during immiscible displacement of oil by water. This diagram has been originally constructed and validated using simulations and experiments conducted on micro-models only. The scale, the geometry and the dimensions of the porous media used here are very different.

On the diagram, the experiments of this study fall in (or at the fringe) of the capillary fingering region, not so far from the viscous fingering region for CF2 to CF5. *M* and *C* values are given Table 5.These predictions are compatible with our observations, but the result of CF1 falling in the same domain as the other experiments is questionable, as it demonstrated a stable front. However the residual oil saturation in the swept zones (around 37%) demonstrates the high capillary forces. The stable displacement region they defined should be seen as a region of near complete oil recovery, reached beyond the standard capillary desaturation curve transition, at very high capillary number. Predictions for CF2 to CF5 are relatively consistent with experimental results, as they show a combination of both viscous and capillary fingering mechanisms. The contribution of the two mechanisms can't be done using the visual inspection only. In the following section, the CT-images has been processed to quantify their contribution alone to the breakthrough earliness.

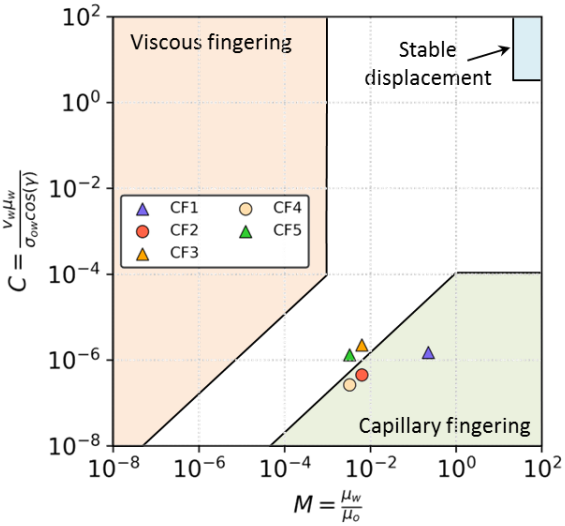

Fig. 13. Corefloods positioning on Lenormand et al [7] fingering domains diagram. *M* and *C* are the dimensionless viscosity and capillary numbers. Circle and triangle markers respectively refer to corefloods conducted at 1.7 and 7.0 cc/min. *M* and *C* values are given Table 5.

Table 5. Viscous and capillary (*M, C*) dimensionless numbers defined by Lenormand et al. $M = \mu_w/\mu_o$ and $C = v\mu_w/\sigma_{ow}cos\theta$, where θ is the contact angle, taken to 0°, water-wet case.

	CF1	CF2	CF3	CF4	CF5
M	2.2E-01	6.3E-03	6.3E-03	3.3E-03	3.3E-03
C	1.5E-06	4.5E-07	2.3E-06	2.7E-07	1.3E-06

3.3 Fingering mechanisms

Following the Lenormand et al. phase-diagram theory [7], the volume of water injected at breakthrough can be expressed as the product of two distinct contributions (see equation 6): (i) the fraction of the core pore volume swept by the water at BT (PV^{swept}) and (ii) the oil-recovery in this swept areas S_o^{swept}. This oil recovery is defined as the fraction of oil produced (or displaced) in the swept areas. The sweeping efficiency PV^{swept} account for fingering observable at macro-scale. The microscopic recovery S_o^{swept} account for the capillary trapping, occurring at the pore-scale. They can be respectively identified as the viscous fingering and the capillary fingering.

$$PV@BT = PV^{swept} * S_o^{swept} \quad (6)$$

The volume swept by the water at a certain time is obtained by subtracting the initial CT-scan (at *Swi*) to the corresponding CT-scan. Swept and unswept areas are segmented using a threshold applied on the subtracted saturations. Fig. 14 shows the core local saturations measured using the CT-scanner during the flooding. Two populations of local saturations can be clearly identified: (1) in red, high oil saturation, corresponding to local *Swi* values and (2) in blue, lower oil saturations defining the swept area. After phases segmentation, the volume swept at BT (PV^{swept}) and the microscopic oil recovery S_o^{swept} in this area are easily derived (see illustration Fig. 15).

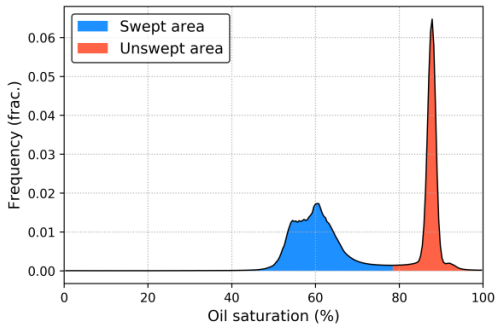

Fig. 14. CT-scan local saturations distribution due core flooding (CF5@14.5%PV. The red and blue areas refer to the unswept and swept areas.

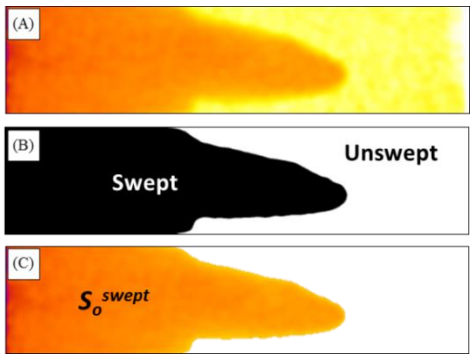

Fig. 15. Swept and unswept areas segmentation (CF5@14.5%PV, sagittal slicing). (A) is the original image, (B) is after swept and unswept areas segmentation (see details in Fig. 14) and (C) is the saturation displayed in the swept area, used to compute the microscopic oil recovery.

PV^{swept} and S_o^{swept} values are computed for all corefloods and summarized Table 6. They are plotted and compared Fig. 16. Plain curves represent constant pore-volume curves: they show the solutions of S_o^{swept} and PV^{swept} resulting in equivalent pore volume at breakthrough (see equation 6). This diagram allows to dissociate the contribution of the waterflood sweeping and the microscopic recovery to better characterized the fingering mechanisms underlying the early BT. Above the $x = y$ diagonal is the region of capillary fingering, with poor microscopic oil recoveries. Below the $x = y$ diagonal is the region of viscous fingering, with poor sweeping efficiencies. High PV^{swept} and S_o^{swept} values is the region of stable displacement.

Table 6. PV^{swept} and S_o^{swept} values measured at BT, respectively quantifying the viscous fingering and the capillary fingering (see equation 6).

	CF1	CF2	CF3	CF4	CF5
S_o^{swept} (%)	51.3	31.5	30.6	30.2	29
PV^{swept} (%)	98.0	88.6	71.9	89.1	66.4

The 5 corefloods show good sweeping efficiency and intermediate to poor microscopic oil recovery. As expected from the piston-like displacement, CF1 coreflood shows a near-perfect sweeping efficiency at BT, with all the remaining oil trapped by capillary forces. The corefloods CF2 to CF5 demonstrate lower microscopic oil recoveries, with a sweeping efficiency close to 90% for experiments conducted at 1.4cc/min and around 70% for the experiments conducted at higher velocity (7cc/min). The strong reduction of microscopic oil recoveries between CF1 and the other cores seems mainly explained by the fluid mobility ratios.

For coreflood CF2 to CF5, the difference in sweeping efficiency at BT is not controlled by the fluids mobility ratio: CF2-CF3 (and CF4-CF5) are conducted using the same fluids but show different sweeping values. It is on the other hand controlled by the injection flow rate. This result illustrates the effect of the flow velocity discussed above for water-wet cores, with the fluids front being less stabilized at increasing flow rates.

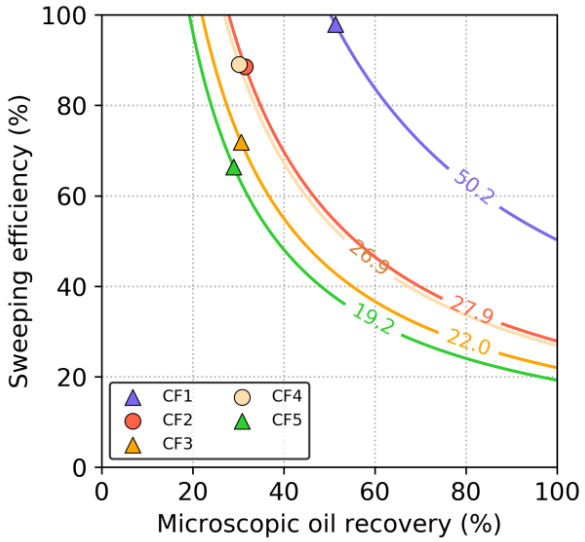

Fig. 16. Sweeping efficiency and microscopic oil recovery at breakthrough (So^{swept} and PI^{swept}). Plain curves are iso-injected pore volume line, plotted for each coreflood (see equation 6). Circle and triangle markers respectively refer to corefloods conducted at 1.7 and 7.0 cc/min.

4. Conclusion

In this study, effect of the oil viscosities and injection flow rates on the water-breakthrough have been investigated using in-situ saturation imaging. It was found that the oil recovery at brine breakthrough (%PV) shows a good correlation with the viscous fingering number as defined by Doorwar [8]. Early water breakthrough appeared boosted by injection flow rate and less favorable fluids mobility ratio.

The local saturation monitoring provides new insight to characterize the finger shapes and analyze the production mechanisms, for the different flowing conditions. In water-wet conditions, the capillary forces contribute to stabilizing the front against viscous instabilities. If the viscous forces become too dominant, the capillary forces are overcome and fingering may occurs for displacement with unfavorable fluids ratio.

A diagram has been constructed to separately quantify the contribution of the viscous fingering and the capillary fingering. Capillary fingering is defined as the fingering occurring at low scale, below the scanner resolution. Viscous fingering is defined as the macroscopic fingering, visible using the CT-images. Our results indicate that although both fingerings were seen in our corefloods, capillary fingering was responsible for more oil trapping than the viscous fingering.

For further work, additional experiments should be conducted to compare the fingering mechanisms for oil-wet or intermediate-wet core.

Acknowledgement

Experiments have been conducted with the technical expertise of M.C. Lynch for the CT-scanner and F. Martin for the corefloods.

References

1. P. van Meurs, C. van der Poel, A Theoretical Description of Water-Drive Processes Involving Viscous Fingering, *SPE-931-G*, **213**, 103-112 (1958)
2. T. K. Perkins, O. C. Johnston, A Study of Immiscible Fingering in Linear Models, *SPE-8371-PA 9*, **01**, 39–46 (1969)
3. J. Hagoort, Displacement Stability of Water Drives in Water-Wet Connate-Water-Bearing Reservoirs, *SPE-8371-PA 14*, **01**, 63–74 (1974)
4. Y. C. Yortsos, A. B. Huang, Linear-Stability Analysis of Immiscible Displacement: Part 1-Simple Basic Flow Profiles, *SPE-12692-PA* 1, **04**, 378–390 (1986)
5. E. J. Peters, D. L. Flock, The Onset of Instability During Two-Phase Immiscible Displacement in Porous Media, *SPE-8371-PA 2*, **02**, 249–258 (1981)
6. R. L. Chuoke, P. van Meurs, C. van der Poel, The Instability of Slow, Immiscible, Viscous Liquid-Liquid Displacements in Permeable Media, *SPE-1141-G,* **216**, 188-194 (1959)
7. R. Lenormand, E. Touboul,C. Zarcone, Numerical models and experiments on immiscible displacements in porous media, *Journal of Fluid Mechanics*, **189**, 165–187 (1988)
8. S. Doorwar, Understanding unstable immiscible displacement in porous media, *Thesis*, University of Texas at Austin (2015)
9. R. D. Loubens, G. Vaillant, M. Regaieg et al., Numerical Modeling of Unstable Water Floods and Tertiary Polymer Floods into Highly Viscous Oils, *SPE-182638-PA*, **23**, (2017)
10. H. Luo, K. K. Mohanty, M. Delshad, Modeling and Upscaling Unstable Water and Polymer Floods: Dynamic Characterization of the Effective Viscous Fingering, *SPE-179648-PA 20*, **04**, 779–794 (2017)
11. T. Worawutthichanyakul, K. K. Mohanty, Unstable Immiscible Displacements in Oil-Wet Rocks, *Transport in Porous Media* **119**, 205–223 (2017)
12. S. Doorwar, K. K. Mohanty, Viscous-Fingering Function for Unstable Immiscible Flows (includes associated Erratum), *SPE-173290-PA 22*, **01**, 19–31 (2017)
13. F. J. Fayers, An Approximate Model With Physically Interpretable Parameters for Representing Miscible Viscous Fingering, *SPE-12692-PA 3*, **02**, 551–558 (1988)
14. J. Sharma, S. B. Inwood, A. Kovscek, Experiments and Analysis of Multiscale Viscous Fingering During Forced Imbibition, *SPE-173290-PA 17*, **04**, 1142–1159 (2012)
15. A. Skauge, P. A. Ormehaug, T. Gurholt et al., 2-D Visualisation of Unstable Waterflood and Polymer Flood for Displacement of Heavy Oil, *Society of Petroleum Engineers*, 12 (2012)

16. D. Pavone, Observations and Correlations for Immiscible Viscous-Fingering Experiments, *SPE-12692-PA* 7, **02**, 187–194 (1992)
17. D. R. F. Harleman, R. R. Rumer, Longitudinal and lateral dispersion in an isotropic porous medium, *Journal of Fluid Mechanics*, **3**, 385–394 (1963)
18. S. Bouquet, S. Leray, F. Douarche, et al., Characterization of Viscous Unstable Flow in Porous Media at Pilot Scale - Application to Heavy Oil Polymer Flooding, *EAGE* (2017)
19. A. Clauset, C. R. Shalizi, M. E. J. Newman, Power-Law Distributions in Empirical Data. *SIAM Rev, 51*, **4**, 661–703 (2009)

Core-scale sensitivity study of CO_2 foam injection strategies for mobility control, enhanced oil recovery, and CO_2 storage

Zachary Paul Alcorn[1*], *Sunniva B.* Fredriksen[1], *Mohan* Sharma[2], *Tore* Føyen[1,3], *Connie* Wergeland[1], *Martin A.* Fernø[1], *Arne* Graue[1], *and Geir* Ersland[1]

[1]Dept. of Physics and Technology, University of Bergen, Norway
[2]National IOR Centre of Norway, University of Stavanger, Norway
[3]SINTEF Industry, Trondheim, Norway

Abstract. This paper presents experimental and numerical sensitivity studies to assist injection strategy design for an ongoing CO_2 foam field pilot. The aim is to increase the success of *in-situ* CO_2 foam generation and propagation into the reservoir for CO_2 mobility control, enhanced oil recovery (EOR) and CO_2 storage. Un-steady state *in-situ* CO_2 foam behavior, representative of the near wellbore region, and steady-state foam behavior was evaluated. Multi-cycle surfactant-alternating gas (SAG) provided the highest apparent viscosity foam of 120.2 cP, compared to co-injection (56.0 cP) and single-cycle SAG (18.2 cP) in 100% brine saturated porous media. CO_2 foam EOR corefloods at first-contact miscible (FCM) conditions showed that multi-cycle SAG generated the highest apparent foam viscosity in the presence of refined oil (*n*-Decane). Multi-cycle SAG demonstrated high viscous displacement forces critical in field implementation where gravity effects and reservoir heterogeneities dominate. At multiple-contact miscible (MCM) conditions, no foam was generated with either injection strategy as a result of wettability alteration and foam destabilization in presence of crude oil. In both FCM and MCM corefloods, incremental oil recoveries were on average 30.6% OOIP regardless of injection strategy for CO_2 foam and base cases (i.e. no surfactant). CO_2 diffusion and miscibility dominated oil recovery at the core-scale resulting in high microscopic CO_2 displacement. CO_2 storage potential was 9.0% greater for multi-cycle SAGs compared to co-injections at MCM. A validated core-scale simulation model was used for a sensitivity analysis of grid resolution and foam quality. The model was robust in representing the observed foam behavior and will be extended to use in field scale simulations.

1. Introduction

A major challenge in carbon dioxide (CO_2) enhanced oil recovery (EOR) is poor macroscopic CO_2 sweep efficiency caused by the low viscosity and density of injected CO_2 [1, 2]. These adverse properties can result in viscous fingering and gravity override, greatly hindering oil recovery and sweep efficiency [3, 4]. Reservoir heterogeneity can also cause injected CO_2 to channel through high permeability zones (layers or fractures) resulting in early CO_2 breakthrough, high CO_2 recycling, and low incremental oil recoveries. CO_2 foam injection is a laboratory verified and field-validated technique proven to mitigate poor CO_2 sweep efficiencies through effectively increasing CO_2 viscosity and reducing its relative permeability [5].

Foam is a dispersion of gas (CO_2, in this case) in liquid where the liquid phase is continuous and at least some of the gas phase is discontinuous and separated by lamella [6]. The discontinuous CO_2 phase becomes trapped between lamella [7], effectively reducing its relative permeability. Foam apparent viscosity is used as a measure of foam strength in laboratory experiments, where a stronger foam corresponds to a higher apparent viscosity. Entrapment of CO_2 in foam and CO_2-surfactant emulsification also increases CO_2 apparent viscosity and reduces CO_2 mobility [8, 9]. These combined effects are capable of diverting flow from high permeability, well-swept regions, into less permeable areas with higher oil saturations, thereby increasing macroscopic displacement and oil recovery.

CO_2 foam generation and stability are influenced by oil composition and wettability. The presence of oil can destabilize some foams [10] and it has also been reported that foam can only be generated at strongly water-wet conditions [11]. At strongly water-wet conditions, water-wet films covering the pore surfaces maintain the continuous foam structure [12]. A shift to oil-wet can cause the lamellas to detach from the pore walls and foam may be destabilized. Schramm and Mannhardt (1996) confirmed reduced foam effectiveness at intermediate to oil-wet conditions [13] and Fredriksen et al. (2019) induced surfactant wettability alteration in oil-wet fractures to generate CO_2 foam in matrix below a critical oil saturation [14]. The impacts of wettability and the presence of oil on foam stability are areas under active investigation.

* Corresponding author: zachary.alcorn@uib.no